Journal of Translational Medicine

RESEARCH

Open Access

Oxidative stress reprograms benign prostatic hyperplasia microenvironments: insights from integrative multi-omics and machine learning

Jie Chen[1†], Jingxing Bai[1†], Bo Chen[1†], Yin Huang[1], Jinze Li[1], Zeyu Chen[1], Biao Ran[1], Qiang Wei[1], Jianzhong Ai[1*], Liangren Liu[1*] and Dehong Cao[1*]

Abstract

Background Oxidative stress (OS) is increasingly implicated in benign prostatic hyperplasia (BPH), yet the underlying cellular programs remain unclear. We integrated multi-omics and machine learning to identify OS-associated biomarkers and to characterize OS-linked stromal states, with targeted experimental validation.

Methods Two bulk transcriptomic datasets (12 BPH, 16 controls) were integrated to identify DEGs and OS-associated DEGs, followed by WGCNA, enrichment analyses, and four machine-learning algorithms to prioritize hub genes and build a diagnostic nomogram. Consensus clustering defined molecular subtypes. Candidate compounds were screened in silico. Single-cell RNA-seq (124,616 cells) and spatial transcriptomics were analyzed for OS scoring, trajectories, and inferred intercellular communication. Experimentally, WPMY-1 prostatic stromal cells were exposed to LPS to induce OS; intracellular ROS (flow cytometry), ACOX2 expression (RT-qPCR/western blot), proliferation (EdU), and apoptosis (Annexin V) were assessed under ACOX2 overexpression or shRNA knockdown. ACOX2 expression in human prostate tissues was evaluated by immunohistochemistry.

Results We identified 499 DEGs and 26 OS-DEGs. Machine learning converged on three upregulated hub genes: ACOX2, CTSB, and SERPINF1, which with diagnostic AUCs of 0.880 (0.753-1.000), 0.828 (0.663–0.993), and 0.854 (0.711–0.997); however, given the modest sample size, these findings should be interpreted as hypothesis-generating. Two BPH subtypes were identified (immune-infiltrated vs. non-immune). Single-cell analyses showed elevated OS scores across cell types, highest in fibroblasts; ACOX2-high fibroblasts were expanded in BPH and exhibited trajectory-associated increases in ACOX2 with enriched inferred signaling (including TNFSF12-TNFRSF12A). Spatial

†Jie Chen, Jingxing Bai and Bo Chen contributed equally to this work.

*Correspondence:
Jianzhong Ai
ajz6363@126.com
Liangren Liu
liuliangren@scu.edu.cn
Dehong Cao
caodehong@scu.edu.cn

Full list of author information is available at the end of the article

transcriptomics revealed regional OS heterogeneity and spatial association of hub-gene expression with OS-enriched areas. In vitro, LPS increased ROS and upregulated ACOX2, ACOX2 overexpression increased proliferation and reduced apoptosis, whereas knockdown showed opposite effects and attenuated LPS-associated proliferative phenotypes. IHC showed stronger ACOX2 staining in hyperplastic vs. normal prostate tissues.

Conclusions These results nominate ACOX2, CTSB, and SERPINF1 as candidate OS-associated markers in BPH and support a hypothesis-generating multi-omics signature that warrants validation in larger independent human cohorts. Experimental perturbation and tissue staining provide validation for an ACOX2-associated activation-like phenotype under OS, motivating biomarker-guided stratification and OS-targeted therapeutic exploration.

Keywords Benign prostatic hyperplasia, Oxidative stress, ACOX2, Fibroblast, Single-cell RNA-seq, Spatial transcriptomics

Introduction

Benign prostatic hyperplasia (BPH) is one of the most common causes of lower urinary tract dysfunction in elderly men, characterized by excessive proliferation of stromal and epithelial cells in the prostate [1]. Globally, the absolute burden of BPH is highest among men aged 65–74 years [2]. With the accelerating pace of population ageing, the clinical demand for BPH-related healthcare is expected to rise exponentially. BPH not only increases healthcare expenditure but also significantly impairs quality of life. Patients are at greater risk of falls and depression, along with marked declines in health-related quality-of-life indices—including sleep quality, psychological well-being, daily functioning, and sexual health—which ultimately compromise social functioning [2].

The underlying mechanisms driving BPH remain poorly understood. Elucidating novel molecular pathways and identifying potential therapeutic targets is therefore of critical importance to address the rising clinical and societal burden of BPH. Several factors—including inflammatory mediators [3], hormones [4], dietary influences, oxidative stress (OS) [5], and genetic predisposition [6]—are implicated in BPH pathogenesis. OS arises when excessive production of highly reactive species, such as reactive oxygen species (ROS) and reactive nitrogen species, overwhelms the antioxidant defense system, thereby inducing tissue injury. Elevated ROS levels accelerate lipid, protein, and nucleic acid damage, while disrupting key signaling pathways that regulate cell survival, proliferation, and inflammation [7]. Accumulating evidence indicates the presence of OS in BPH [8, 9]. For instance, ROS generated by chronic prostatitis may alter DNA repair mechanisms, promote point mutations, deletions, or rearrangements, and disrupt programmed cell death, thereby driving hyperplastic states [10]. In BPH-1 cells, neferine has been shown to activate Nrf2 and its downstream proteins, suppressing ROS and enhancing antioxidant defenses [11]. Despite these insights, most existing studies merely confirm the occurrence of OS in BPH, without defining specific molecular markers or delineating the precise mechanisms involved.

Against this backdrop, the present study provides a comprehensive assessment of the interplay between OS and BPH across bulk-RNA sequencing (bulk-RNA-seq), single-cell transcriptomics sequencing (scRNA-seq), and spatial transcriptomics sequencing. Our aim is to identify robust biological markers and to clarify their mechanistic roles in the initiation and progression of prostatic hyperplasia.

Materials and methods

Dataset collection and processing

We utilized the Gene Expression Omnibus (GEO) database (https://www.ncbi.nlm.nih.gov/geo) to access the GSE7307 and GSE119195 bulk-RNA set, which included seven BPH and 13 normal prostate samples from GSE7307 dataset, five BPH and three normal prostate samples were obtained from the GSE119195 dataset. We performed an independent cross-species validation in rodent BPH models by integrating two public bulk RNA-seq datasets (GSE218403 and GSE217800) after ortholog mapping and batch adjustment, yielding 6 BPH and 6 normal prostate samples as an external test set. OS-related metabolic genes were obtained from a previous study [12], which contained 807 genes (literature-derived). To reduce dependence on a single literature-derived OS list and to improve reproducibility, we incorporated curated oxidative-stress–related gene sets from the Molecular Signatures Database (MSigDB). Specifically, we used HALLMARK_REACTIVE_OXYGEN_SPECIES_PATHWAY (Hallmark ROS) and GOBP_RESPONSE_TO_OXIDATIVE_STRESS (GO:0006979) as reference OS gene sets, in addition to our previously used literature-derived OS gene list. Gene set unification was performed by taking the union of all five gene sets, followed by removal of duplicates, resulting in 1,060 unique OS-related genes for subsequent analyses. The full gene members for each gene set are provided in Supplementary Table 1. The integrated BPH expression data was obtained by removing batch effect of two BPH datasets based on the combat function of "SVA" package [13] in R software (version 4.3.1), which finally contained

12 BPH samples and 16 control samples. All datasets utilized in this study could be found in Supplementary Table 2.

Differential genes expression analysis and signature identification

Differentially expressed genes (DEGs) from integrated datasets were discovered using the "Limma" R package. Genes with logFC > 1 and $p < 0.05$ were defined as upregulated, while those with logFC < − 1 and $p < 0.05$ were considered downregulated. Subsequently, the distribution of DEGs was displayed using volcano plots generated with the "ggvolcano" package.

Weighted Gene Co-Expression Network Analysis (WGCNA) and key module genes identification

WGCNA was applied to detect clusters of co-expressed genes, evaluate the relationships among modules and their correlation with clinical traits, and screen for potential biomarkers or therapeutic targets. In this study, networks were constructed with the "WGCNA" package in R, and a soft-threshold power of β = 8 was chosen to ensure scale-free topology. Genes within the key modules were intersected with DEGs and oxidative stress-related genes, and the overlapping genes were defined as oxidative stress-associated DEGs.

Functional enrichment analysis

To explore the biological roles and mechanisms of the pathogenic genes in BPH, Gene Ontology (GO) and Kyoto Encyclopedia of Genes and Genomes (KEGG) analyses were conducted using the "clusterProfiler" package [14]. These analyses covered biological processes (BP), molecular functions (MF), cellular components (CC), and signaling pathways.

The construction of protein–protein interaction (PPI) network

The STRING database (STRING: functional protein association networks) was exploited to establish protein-protein interaction (PPI) networks with a medium confidence score of > 0.15, which Cytoscape then visualized.

Screening hub genes by machine learning

To pinpoint the most representative genes associated with oxidative stress, four machine learning approaches were employed. Least Absolute Shrinkage and Selection Operator (LASSO) regression was used to eliminate irrelevant features by applying an L1 penalty. LASSO regression was performed using 10-fold cross-validation (implemented by "cv.glmnet" function with parameter nfolds = 10) to select the optimal lambda value by minimizing binomial deviance. Cross-validation was repeated five times to stabilize the results. Random Forest (RF), a tree-based algorithm, ranked gene importance based on variable contribution scores. The random forest model was implemented with the use of repeated 10-fold cross-validation (five replicates) with the use of the caret package to assess the importance of variables and reduce the risk of overfitting. Support Vector Machine–Recursive Feature Elimination (SVM-RFE) identified key genes by iteratively removing the least informative features. SVM-RFE: A 5-fold cross-validation (parameter k = 5) was integrated into the recursive elimination process using the "rfe" function from the "caret" package. The feature set that yielded the highest average cross-validation accuracy was selected. Finally, the Boruta algorithm confirmed robust features by comparing the Z-score of each variable against randomized "shadow" features. The Boruta algorithm, which is inherently robust due to its use of shadow features, was run with 1000 iterations (maxRuns = 1000). The importance of each attribute was calculated based on the Z-score, providing an internal validation mechanism. Genes consistently selected across all methods were considered hub genes.

To avoid information leakage given the small bulk sample size (12 BPH vs. 16 controls), predictive performance was estimated using a nested, repeated, stratified cross-validation framework. In each repetition, the data were split into an outer stratified K-fold CV to obtain held-out predictions. Within each outer training fold, all preprocessing and model selection steps were performed using training data only, including (i) any feature filtering/selection (e.g., LASSO/Boruta/SVM-RFE), (ii) hyperparameter tuning (if applicable) via an inner stratified CV, and (iii) scaling/normalization steps. The outer test fold was not used at any stage until final prediction. Model performance (AUC) was then computed from the concatenated out-of-fold predictions across the outer folds (and across repeats), and 95% confidence intervals were derived using the DeLong method. The final reported AUCs in the main text therefore reflect held-out testing rather than in-sample performance.

Nomogram construction

To enhance the signature's prediction accuracy in BPH patients, we developed a nomogram incorporating relevant clinicopathological factors as well as the risk score derived from the signature. The nomogram and the calibration curves were constructed using the regplot (v 1.1), survival (v 3.5-7), and rms packages (v 6.7-1). We then conducted Decision Curve Analysis (DCA) using the caret package (v 6.0–94) and visualized the results with the ggDCA (v 1.2) package.

Recognition of molecular subtypes

The "ConsensusCluster Plus" R package was used for unsupervised clustering. For ten rounds, 80% of the data

were resampled and 1-Pearson correlation distances were used to accomplish agglomerative BPH clustering. Gene expression levels from microarray data served as the cluster analysis's input files. Visualization of the expression patterns of hub genes across different molecular subtypes was performed using the R package "pheatmap", with a heatmap-type display. Similarly, the "limma" package in R language was used to obtain differentially expressed genes between different subtypes, and then the "ggvolcano" package was used to visualize the volcano map of differentially expressed genes.

Immune-related analysis

Single sample gene set enrichment analysis (ssGSEA) was performed using the "GSVA" (version 1.48.3) software package in R language. First, the immune cell infiltration and immune function scores of each sample were calculated based on the expression matrix of the two clusters. Second, differences in the proportion of immune cell infiltration and immune function scores between the two subtypes were compared using the "reshape2" (version 1.4.4) package in R. Finally, the "ggpubr" (version 0.6.0) package is used to visualize the results as box plots.

Drug prediction and molecular docking

Predicting protein-drug interactions is crucial in comprehending the structural characteristics recommended for receptor sensitivity. ACOX2, SERPINF1 and CTSB have been uploaded Enrichr online web site (https://maayanlab.cloud/Enrichr/), select disease/drug, Click the Drug Signatures Database (DSigDB), which contains 165 possible sensitive drugs (Supplementary Table 3). Candidate drugs were ranked in the ascending order of their adjusted p-values. An adjusted p-value < 0.05 was deemed statistically significant. The three-dimensional structure models of the proteins CTSB and SERPINF1 were obtained from the UniProt database (https://www.uniprot.org/). Chemical structures of candidate compounds (e.g., quercetin) were downloaded from PubChem (https://www.ncbi.nlm.nih.gov/pccompound) in SDF format and converted to PDBQT using AutoDockTools (version 1.5.7). Ligands were protonated and energy-minimized using default settings where applicable. Grid boxes were defined to encompass the putative binding region of the receptor; given the absence of a well-established binding pocket for some targets, we used a receptor-covering grid strategy (default settings) to avoid arbitrary pocket selection. Docking outputs were summarized using predicted binding affinity scores, which were used for prioritization rather than inference of therapeutic efficacy.

scRNA-seq dataset analysis

The scRNA-seq dataset GSE172357 (13 BPH, 6 normal prostate samples) was processed using Seurat (v5.4.0). Cells with 250–5000 detected genes, < 10% mitochondrial, and < 1% hemoglobin gene expression were retained; doublets were removed with DoubletFinder. Data were normalized with SCTransform, and dimensionality reduction was performed by PCA (top 40 PCs) followed by clustering (resolution 0.7) and UMAP visualization. Cluster-specific markers were identified with FindAllMarkers and cell types annotated using canonical markers (Supplementary Table 4). We computed OS activity using four scoring approaches (AUCell, UCell, Seurat AddModuleScore, and ssGSEA applied to aggregated expression), using multiple OS gene sets (Hallmark ROS and GO:0006979, plus literature-derived list). Concordance across gene sets and across scoring methods was quantified by Spearman correlation at both single-cell and aggregated sample levels.

Re-evaluation of signature genes at the cellular level

Signature genes identified from bulk-RNA-seq analyses were evaluated in scRNA-seq datasets to determine their distribution across cell subtypes and their potential role in OS regulation.

Trajectory analysis and intercellular communication

Cell trajectories were reconstructed with Monocle 2, and hallmark pathway enrichment was assessed using Molecular Signatures Database (MSigDB). Intercellular communication was inferred with CellChat based on receptor–ligand interactions, enabling detection of cell type–specific signaling modules.

Spatial transcriptomics analysis

Spatial transcriptomic data (GSE278936) were re-analyzed in Seurat (v5.4.0). After quality control, data were normalized with SCTransform and integrated using Harmony. OS scores were computed with AddModuleScore and GSVA, and spatial expression patterns were visualized using SpatialFeaturePlot.

Deconvolution of cellular composition with spacexr

To infer spatial coordinates of cell types, we integrated ST and scRNA-seq expression profiles using the spacexr R package. Cell type deconvolution was performed with the robust cell type decomposition (RCTD) method, enabling the identification of spatial distributions and cell type–specific differential expression patterns. To independently validate the deconvolution-based mapping, we applied BayesSpace to the same ST section to infer spatial expression domains ($q = 7$). Because BayesSpace domains are not equivalent to discrete cell types, agreement was evaluated at the domain level by (i) cluster × cell-type contingency matrices with row-wise normalized proportions and (ii) weighted cluster purity, defined as the

fraction of spots in each BayesSpace domain assigned to the dominant RCTD cell type.

Cell culture

The WPMY-1 cell line was purchased from Servicebio (Wuhan, China). WPMY-1 cells were cultured in DMEM medium (Sperikon Life Science & Biotechnology, Sichuan, China) supplemented with 5% fetal bovine serum (FBS; Vazyme, Nanjing, China) and 1% antibiotic-antimycotic solution (HyClone, Massachusetts, USA). Cells were incubated at 37℃ in a humidified atmosphere containing 5% CO2. All culture protocols were performed in accordance with the manufacturers recommendations to ensure optimal cell viability and reproducibility. To model oxidative-stress conditions in prostate stromal fibroblasts, WPMY-1 cells were treated with H_2O_2 at a final concentration of 400 μM for 8 h as a canonical oxidative-stress inducer. In parallel, to better mimic the inflammatory milieu relevant to BPH, cells were stimulated with Lipopolysaccharide (LPS; Neobioscience, Shenzhen, China) (20 μg/mL, 48 h) as an inflammatory/ROS-associated stress stimulus that can elevate intracellular ROS downstream. Additionally, knockdown plasmids for ACOX2 and scramble shRNA (Supplementary Table 5), as well as the ACOX2 overexpression plasmid and empty vector (Supplementary Fig. 1AB, miaolingbio, Wuhan, China), were transfected into WPMY-1 cells using Lipo8000 (Beyotime, Shanghai, China).

Flow cytometry analysis

WPMY-1 cells were seeded into 6-well plates at a density of 1×10^5 cells per well and exposed to LPS at concentrations of 0–20 μg/mL for 48 h [15]. Following treatment, the cells were harvested, and apoptosis was assessed using an Annexin V-APC Reagent kit (Elabscience, Wuhan, China) and flow cytometry. Furthermore, to detect intracellular ROS, the treated cells were incubated with a 10 μM dihydroethidium probe (Elabscience, Wuhan, China) in working solution of Reagent 1 at 37 °C in the dark for 30 min. The cells were subsequently washed twice with the working solution of Reagent 1, subjected to trypsin digestion, and resuspended in the working solution for subsequent analysis. A CytoFLEX flow cytometer (Beckman Coulter, USA) was used to evaluate the levels of apoptosis and ROS in the treated cells.

EdU proliferation assay

Cell proliferation was assessed using an EdU assay kit (Elabscience, Wuhan, China). Briefly, cells were seeded into 96-well plates at a density of 2.5×10^3 cells per well and cultured for 24 h. After completing the respective interventions, the culture medium was replaced with fresh medium containing 50 μM EdU, followed by incubation for an additional 2 h. Subsequently, fluorescence labeling was performed according to the manufacturer's instructions. After washing with PBS, nuclei were counterstained with DAPI. Imaging and analysis were conducted using a Celigo image cytometer (Nexcelom, Boston, USA).

Quantitative real-time PCR

Total RNA was extracted using an RNA isolation kit (Vazyme, Nanjing, China). Subsequently, 1 μg of RNA was reverse-transcribed into cDNA using a cDNA synthesis kit (Vazyme, Nanjing, China). Quantitative real-time PCR (RT-qPCR) was performed with a SYBR Green PCR kit (Vazyme, Nanjing, China) on a CFX96 Touch Real-time PCR Detection System (Bio-Rad, CA, USA). β-actin was used as the housekeeping gene for normalization, and relative mRNA expression was quantified using the $2^{-}\Delta\Delta Ct$ method. The sequences of all primers used are listed in the Supplementary Table 6.

Western blot analysis

WPMY-1 cell pellets were thoroughly lysed using ice-cold RIPA buffer (Beyotime, Shanghai, China) supplemented with protease and phosphatase inhibitors (AbMole, Shanghai, China). The lysates were then centrifuged at 12,000 rpm for 30 min at 4 °C. Equal amounts of protein (25 μg) were loaded onto 4%–12% SDS-PAGE gels (Epizyme, Shanghai, China), followed by electrophoresis and subsequent transfer onto PVDF membranes (Millipore, MA, USA). After blocking with 5% skim milk, the membranes were incubated with primary antibodies overnight at 4 °C, followed by incubation with HRP-conjugated secondary antibodies for 1 h at room temperature. Protein bands were visualized using an enhanced chemiluminescence (ECL) kit (Oriscience, Chengdu, China) and imaged with a ChemiDoc MP system (Bio-Rad, CA, USA). In addition to ACOX2, the extracellular matrix–associated marker fibronectin (FN1) was assessed by western blot in the indicated conditions (LPS ± shACOX2), with β-actin as the loading control. β-actin was used as the internal loading control for normalization. Detailed information regarding the specific antibodies used is provided in the Supplementary Table 7.

Immunohistochemical staining

Immunohistochemical staining was performed to evaluate the expression of ACOX2 in normal human prostate tissues and hyperplastic human prostate tissues. Prostate tissue sections were deparaffinized, rehydrated, permeabilized, and blocked according to the instructions of the immunohistochemistry kit (Elabscience, Wuhan, China). The sections were then incubated overnight at 4 °C with a primary antibody against ACOX2 (1:200), followed by

incubation with poly-HRP anti-rabbit IgG for 60 min at room temperature. Subsequently, DAB staining and hematoxylin counterstaining were carried out. Images were captured using a Zeiss microscope (Zeiss, Jena, Germany).

Statistical analysis

All statistical procedures were performed in R. Group comparisons were conducted using the Wilcoxon rank-sum test, while associations between variables were assessed with Spearman's correlation. A two-sided $p < 0.05$ was regarded as statistically significant.

Results

Identification of DEGs and OS-DEGs between BPH and normal prostate tissues

We first constructed an integrated dataset comprising 12 BPH and 16 control prostate tissue samples from GSE7307 and GSE119195, with batch effects removed to generate a unified expression profile (Supplementary Fig. 2AB). Volcano plot analysis identified 323 upregulated and 176 downregulated differentially expressed genes (DEGs) (Supplementary Fig. 2C; Supplementary Table 8). Weighted gene co-expression network analysis (WGCNA) was applied to identify modules associated with BPH. With the soft-threshold power β set to 8 (Fig. 1A), 25 modules were delineated (Fig. 1C), among which the grey60 module showed the strongest association with BPH (Fig. 1B, D). To refine our results, we overlapped DEGs, module genes, and oxidative stress (OS)-related genes using Venn analysis, yielding 26 shared genes (Fig. 1E).

Functional enrichment analysis

To elucidate the biological roles of the 26 overlapping genes, we performed KEGG and GO enrichment analyses (Supplementary Fig. 3A, B). GO analysis revealed enrichment in regulation of peptidase activity and response to oxidative stress within the biological process (BP) category; platelet alpha granule and collagen-containing extracellular matrix within the cellular component (CC) category; and ferrous iron binding and electron transfer activity within the molecular function (MF) category. KEGG pathway analysis highlighted enrichment of oxidative stress–related pathways, including HIF-1 signaling and ferroptosis, which are consistent with potential involvement of OS-associated programs in BPH. STRING-based protein–protein interaction (PPI) analysis revealed a highly interconnected network among these hub genes (Supplementary Fig. 3C, D).

Identification and validation of diagnostic biomarkers using bioinformatics and machine learning

To identify OS-related diagnostic biomarkers for BPH, we applied four machine learning algorithms. Random forest (RF) identified the top 15 candidate genes (Fig. 2A, B), support vector machine–recursive feature elimination (SVM-RFE) selected 4 key genes (Fig. 2C, D), Boruta identified 11 significant variables after 500 iterations (Fig. 2E, F), and least absolute shrinkage and selection operator (LASSO) regression identified 4 genes (Fig. 2G, H). Intersecting these results revealed three robust hub genes—ACOX2, CTSB, and SERPINF1 (Fig. 2I; Supplementary Table 9)—all of which were upregulated in BPH. Receiver operating characteristic (ROC) analysis demonstrated strong diagnostic performance, with AUCs of 0.880 (0.753-1.000) for ACOX2, 0.828 (0.663–0.993) for CTSB, and 0.854 (0.711–0.997) for SERPINF1 (Fig. 2J–L). In external validation, we did not re-train or re-select features. Instead, as supportive evidence, we performed a cross-species validation using integrated rodent BPH datasets ($n = 6$ BPH vs. 6 controls). The OS-associated signature showed consistent directionality and retained discriminative ability in this setting (Supplementary Fig. 2D-I), supporting cross-species generalizability; however, this analysis does not substitute for an independent human validation cohort due to species and disease-model differences and the limited sample size. A nomogram constructed with these genes showed excellent calibration (Fig. 2M, N) and predictive power for distinguishing BPH from controls (AUC = 0.922) (Fig. 2O).

Molecular subtypes of BPH

Consensus clustering based on the three hub genes separated BPH samples into two molecular subtypes: Cluster 1 (C1) and Cluster 2 (C2) (Supplementary Fig. 4A, B). ACOX2, CTSB, and SERPINF1 were consistently upregulated in C2 (Supplementary Fig. 4C). Differential expression analysis identified 1,535 upregulated and 2,320 downregulated genes between the two clusters (Supplementary Table 10; Supplementary Fig. 4D). GO enrichment revealed that upregulated genes in C2 were significantly enriched in immune-related processes, including activation of immune response, negative regulation of immune system process, and regulation of innate immune response (Supplementary Fig. 4E), whereas downregulated genes were enriched in neuronal processes, such as axon development (Supplementary Fig. 4F). These findings suggest that C2 represents an immune-infiltrated subtype, whereas C1 is non-immune infiltrated, a hypothesis supported by immune infiltration and functional analyses (Supplementary Fig. 5A, B).

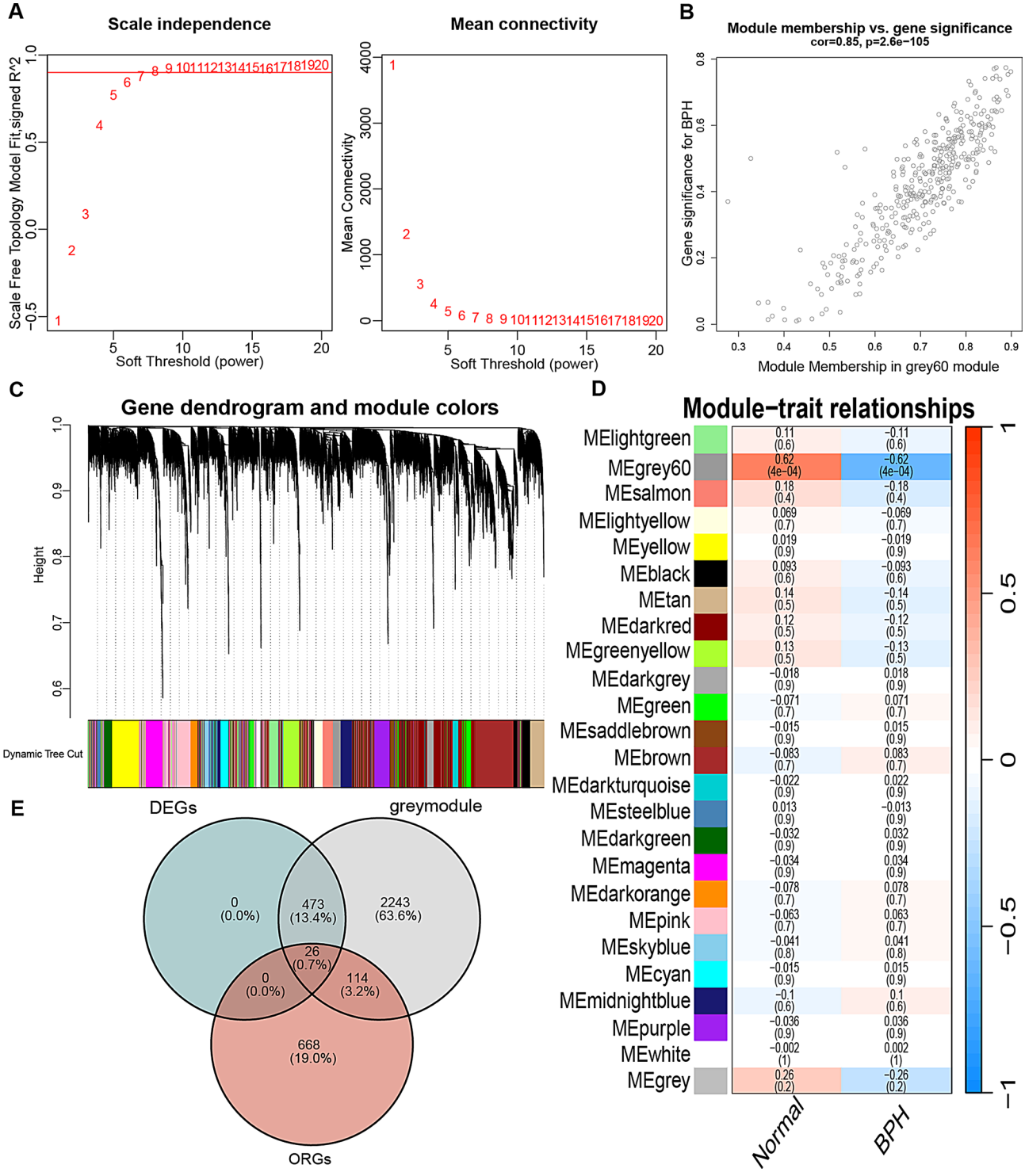

Fig. 1 Identification of BPH-related modules using WGCNA. (**A**) Network topology analysis of the soft-thresholding power (β). (**B**) Scatter plot depicting the association between gene significance and module membership in the grey60 module. (**C**) Hierarchical clustering of differentially expressed genes (DEGs) based on multiple metrics. (**D**) Module–trait correlations. (**E**) Overlap between genes in the grey60 module, oxidative stress–related genes, and DEGs

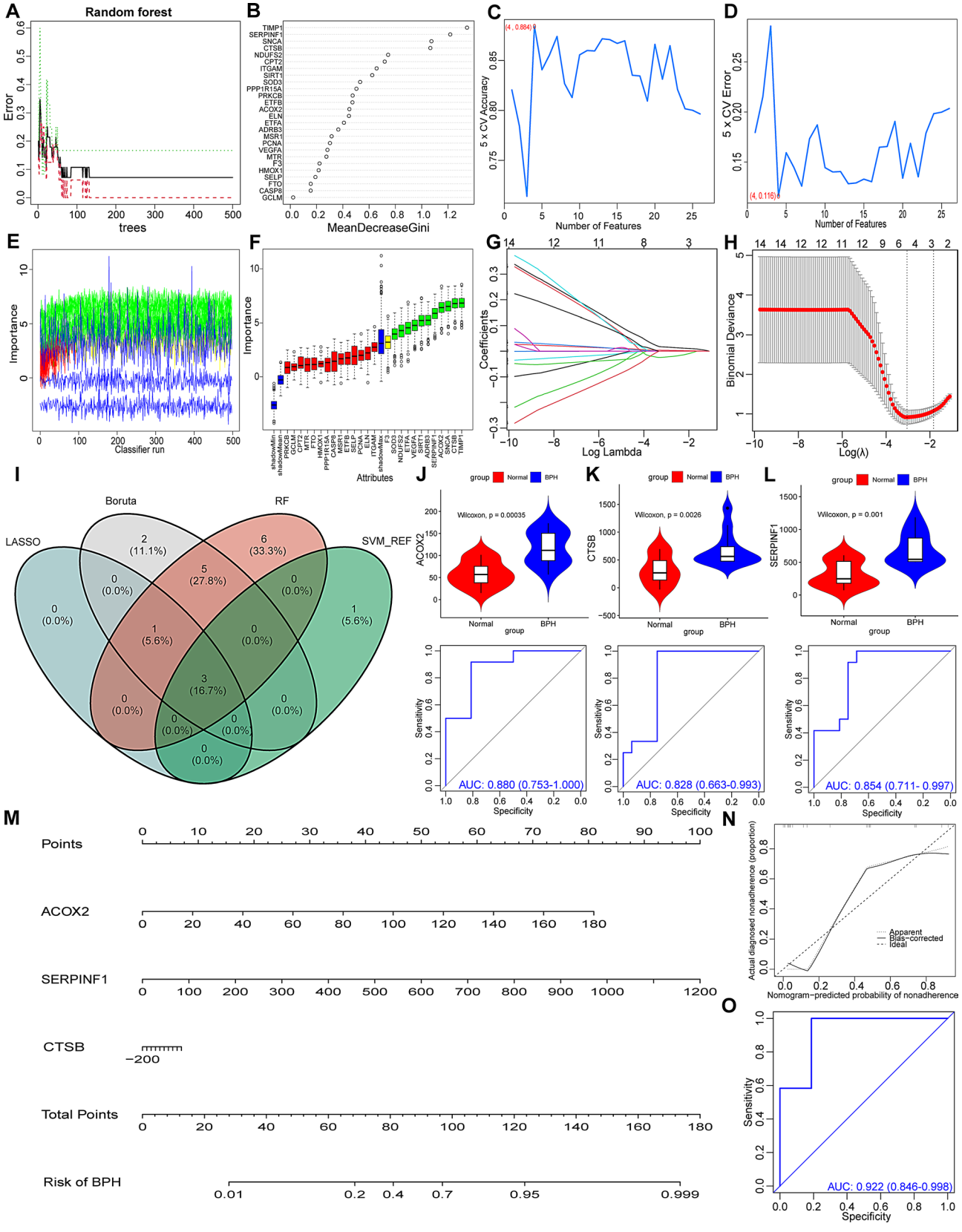

Fig. 2 (See legend on next page.)

(See figure on previous page.)

Fig. 2 Identification and validation of oxidative stress–related DEGs. (**A**, **B**) Key genes identified by random forest. (**C**, **D**) Four key genes identified using support vector machine–recursive feature elimination (SVM-RFE). (**E**, **F**) Key genes identified using the Boruta algorithm. (**G**, **H**) Key genes identified using least absolute shrinkage and selection operator (LASSO) regression. (**I**) Three hub genes (ACOX2, CTSB, and SERPINF1) identified by the overlap of four machine learning approaches. (**J**–**L**) Expression levels and ROC curves of ACOX2, CTSB, and SERPINF1 in BPH samples. (**M**) Nomogram based on ACOX2, CTSB, and SERPINF1 for predicting BPH risk. (**N**) Calibration curve of the nomogram. (**O**) ROC curve analysis of the nomogram

Drug prediction and molecular docking

To identify potential therapeutics for the immune-infiltrated subtype, we performed molecular docking simulations targeting CTSB and SERPINF1. A total of 165 candidate compounds were retrieved from Enrichr. Quercetin exhibited binding energies of − 7.9 kcal/mol with CTSB and − 7.3 kcal/mol with SERPINF1 (Supplementary Fig. 6A, C), while cyclosporin showed − 5.6 kcal/mol and − 5.9 kcal/mol, respectively (Supplementary Fig. 6B, D). Quercetin showed favorable predicted docking scores with CTSB and SERPINF1, suggesting plausible interactions that warrant further experimental validation.

Single-cell characterization of molecular features in BPH

After stringent quality control, 124,616 high-quality cells from GSE172357 were retained for analysis (Supplementary Fig. 7A–C). PCA on 3,000 highly variable genes (Fig. 3A) yielded 40 principal components for downstream analysis (Supplementary Fig. 7D–G), leading to the identification of 23 clusters (Fig. 3D). Manual annotation using canonical markers (Supplementary Table 4) revealed nine major cell types (Fig. 3B–E). Use the 'FindCluster' function for clustering, and set the resolution parameter to 0.7 (Supplementary Fig. 7H). Differential expression analysis across these cell types (Supplementary Table 11) highlighted distinct transcriptional signatures (Supplementary Fig. 7I). Proportional analysis revealed shifts in cell type composition between BPH and normal tissues (Fig. 3F–H). OS scoring across four algorithms (AUCell, ssGSEA, AddModuleScore, UCell) showed consistently higher OS levels in BPH, particularly in fibroblasts and macrophages (Fig. 3I, J). To assess robustness against OS gene-set selection and scoring algorithms, we computed OS activity using three gene sets (literature-derived, Hallmark ROS, and GO:0006979) and four scoring approaches (AUCell, UCell, AddModuleScore, and pseudobulk ssGSEA aggregated by sample). At the sample level, concordance across scoring approaches within each gene set ranged from $\rho = 0.25–0.83$, with the strongest agreement observed for GO:0006979 ($\rho = 0.51–0.83$), supporting the robustness of OS activation patterns when curated, broader OS definitions are used (Supplementary Fig. 8A-I). Notably, ACOX2, CTSB, and SERPINF1 were broadly expressed across multiple cell types (Fig. 4A–C).

Molecular heterogeneity of fibroblasts in BPH

To explore fibroblast dynamics, we performed pseudotime trajectory analysis, which revealed a continuous differentiation process from resting to activated states, shared between BPH and normal tissues (Fig. 4D, E). Genes with expression > 0.005 and actual dispersion greater than or equal to expected dispersion were retained for subsequent analysis (Fig. 4F). Figure 4G shows the pseudotime distribution of fibroblasts in the UMAP dimensionality reduction space. Figure 4H illustrates the distribution of the AUCell oxidative stress scores of fibroblasts in the UMAP dimensionality reduction space. OS scores remained persistently higher in BPH fibroblasts throughout the trajectory (Fig. 4I). Using pseudo-bulk DE testing with edgeR and BH-FDR correction ($q < 0.05$), we identified 1,144 upregulated and 471 downregulated genes between BPH and controls in fibroblasts (Supplementary Table 12; Fig. 4J). GO (Supplementary Fig. 7J) and KEGG analysis (Fig. 4K) using the 1,144 up-regulated genes showed that more genes were up-regulated than lipid and atherosclerosis and toll-like receptor signaling pathway. Cross-referencing upregulated genes with OS-related genes and bulk-RNA-seq hub genes prioritized ACOX2 as a fibroblast-associated gene, with expression showing a progressive increase along pseudotime in BPH fibroblasts (Figs. 4L and 5A).

Intercellular communication in fibroblast subpopulations

CellChat analysis predicted that ACOX2$^+$ fibroblasts had the highest inferred communication strength within the BPH microenvironment (Fig. 5B, C). These fibroblasts were positioned centrally in the inferred signaling network, with pathways related to angiogenesis, extracellular matrix remodeling/fibrosis, and immune modulation enriched among predicted interactions (Fig. 5D). In particular, the TNFSF12–TNFRSF12A axis was prioritized as a candidate interaction axis warranting further investigation. Compared with ACOX2$^-$ fibroblasts, ACOX2$^+$ fibroblasts displayed greater outgoing signaling strength (Fig. 5E). Differential expression and GSEA further revealed enrichment of metabolic pathways including peroxisome metabolism, PPAR signaling, fatty acid oxidation, and bile acid synthesis (Fig. 5F; Supplementary Tables 13–14).

Pseudotime analysis of ACOX2$^+$ fibroblast subtypes

To further investigate the molecular diversity within fibroblasts, we isolated fibroblast populations and

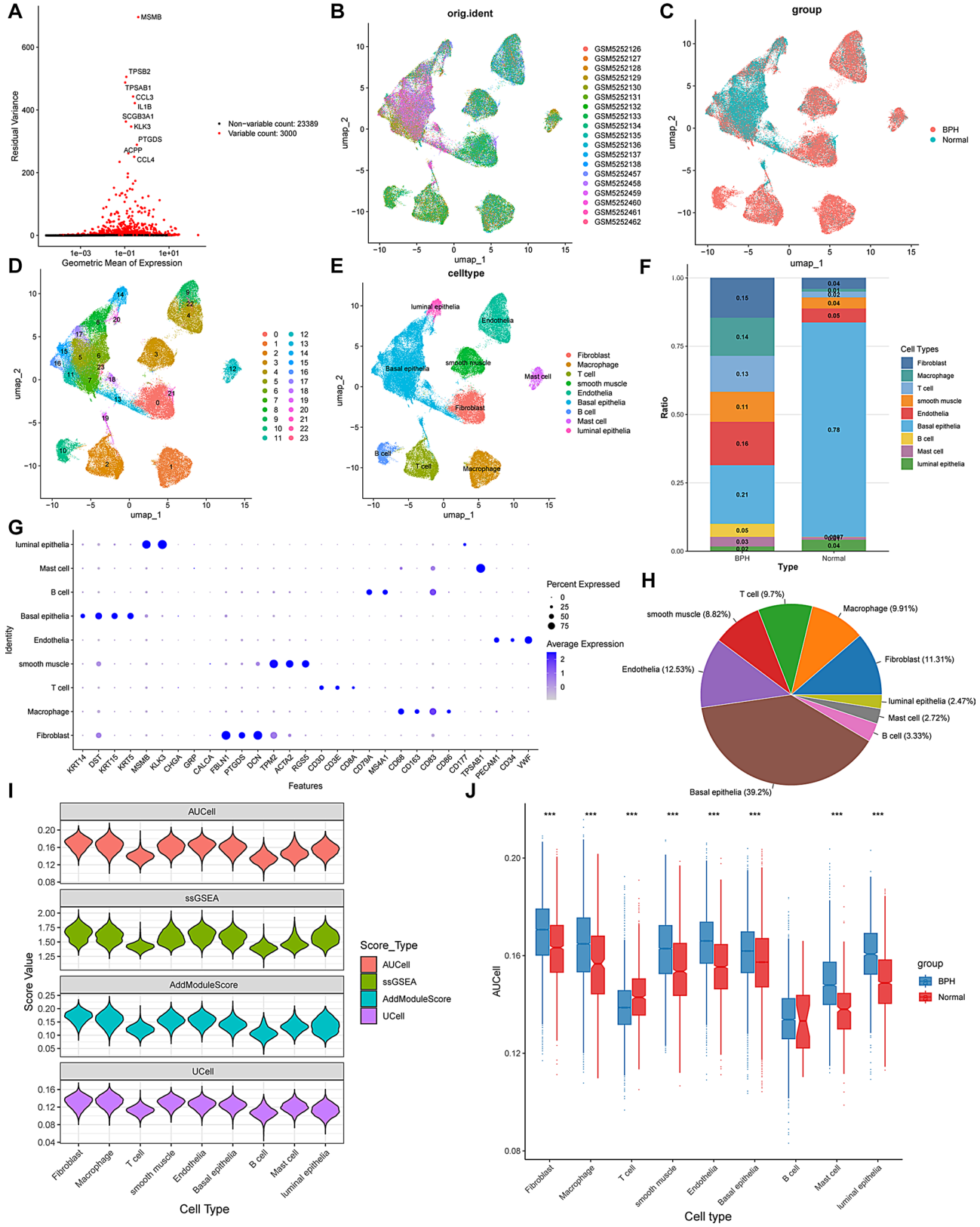

Fig. 3 (See legend on next page.)

(See figure on previous page.)

Fig. 3 Single-cell profiling of molecular features in BPH. (**A**) Selection of 3,000 highly variable genes for analysis. (**B**) UMAP overview of 19 samples. (**C**) UMAP colored by BPH versus normal controls. (**D**) UMAP colored by 23 clusters. (**E**) UMAP colored by cell types. (**F**) Cell type proportions in BPH versus normal prostate tissues. (**G**) Bubble plot of marker genes for nine major cell types. (**H**) Cell type proportions across all samples. (**I**) Oxidative stress activity across cell types, showing highest scores in fibroblasts and macrophages and lowest in T cells. (**J**) Cell type–specific oxidative stress activity in BPH versus normal tissues

performed de novo clustering based on different gene expression profiles. De novo clustering of fibroblasts identified nine distinct subclusters, including an ACOX2⁺ fibroblast population (Fig. 6A, B). Compared with normal prostate tissues, BPH samples showed an expansion of the ACOX2⁺ fibroblast cluster and depletion of the Fib C5 cluster (Fig. 6D). Pseudotime analysis suggested a trajectory in which early-stage fibroblasts (Fib C1, C2, C7) progressively transitioned into activated ACOX2⁺ fibroblasts (Fig. 6C, E). This differentiation process could be divided into seven stable states (Fig. 6F), with ACOX2⁺ fibroblasts enriched toward terminal branches, consistent with a profibrotic-like transcriptional state in BPH (Fig. 6G). Spatial transcriptomics analysis was associated with spatial co-localization between ACOX2/CTSB/SERPINF1 expression and OS scores in hyperplastic glandular regions (Fig. 6H). To infer the cellular context of these regions, we performed RCTD-based deconvolution using the scRNA-seq reference annotated at the "celltype" level. The inferred dominant cell-type map suggested that epithelial-dominant and stromal-enriched regions formed distinct spatial patterns (Supplementary Fig. 9A). To mitigate potential effects of mixed Visium spots, we defined high-confidence spots (maximum cell-type weight ≥ 0.6) and confirmed that the overall spatial patterns were preserved in this subset (Supplementary Fig. 9B). In parallel, we mapped the second-largest cell-type weight per spot as a proxy of compositional mixing; elevated values were spatially restricted to specific regions, consistent with expected spot-level mixture in Visium data (Supplementary Fig. 9C). Finally, we validated the robustness of deconvolution-based mapping using BayesSpace spatial clustering (q = 7). Domain-level enrichment analysis showed that several BayesSpace domains were strongly dominated by luminal epithelia (row proportions 0.92-1.00), while other domains were enriched for stromal components (e.g., fibroblast and smooth muscle) or mixed epithelial-stromal compositions (Supplementary Fig. 9D). The overall weighted cluster purity was 0.685, supporting substantial agreement between independently inferred spatial domains and the dominant cell-type assignments from RCTD at the domain level. To provide anatomical context for the spatial transcriptomics data, we performed histopathological annotation on the associated H&E images. Since the public dataset did not specify the prostatic zonal origin of each section, we annotated tissue regions based on discernible histological structures rather than presuming zones. Specifically, gland-rich epithelial areas, stroma/smooth-muscle–rich areas, vascular structures, and focal inflammatory aggregates (when identifiable) were marked on the H&E image with spot overlay (Supplementary Fig. 9E). Dynamic expression analysis along pseudotime identified additional genes critical for BPH progression (Fig. 6I).

Experimental validation supports an ACOX2-linked pro-activation phenotype of prostatic stromal cells under oxidative stress

To clarify the oxidative-stress modeling strategy, we first used H_2O_2 as a canonical oxidative-stress inducer in WPMY-1 cells. DHE–flow cytometry confirmed that H_2O_2 treatment increased intracellular ROS (Supplementary Fig. 10A), and ACOX2 protein expression was concomitantly upregulated (Supplementary Fig. 10B), indicating that ACOX2 is ROS-responsive under a canonical oxidative-stress condition. We next employed LPS stimulation to model an inflammatory/ROS-associated stress context that is more reflective of the BPH microenvironment. LPS similarly increased intracellular ROS and induced ACOX2 expression (Supplementary Fig. 10CD), and was therefore used in subsequent functional assays. Functionally, LPS treatment increased EdU incorporation (Supplementary Fig. 10E), indicating enhanced proliferative activity, whereas the overall apoptosis rate showed no significant change compared with the control condition (Supplementary Fig. 10F).

To determine whether ACOX2 is functionally linked to stromal cell activation-like phenotypes, we manipulated ACOX2 expression in WPMY-1 cells (Fig. 7 AB). ACOX2 overexpression increased EdU-positive cell proportion (Fig. 7C) and reduced apoptosis (Supplementary Fig. 10G), while ACOX2 knockdown produced the opposite effects, decreasing proliferation (Fig. 7D) and increasing apoptosis (Supplementary Fig. 10I). Importantly, under oxidative stress conditions (LPS), ACOX2 knockdown attenuated the LPS-associated increase in proliferation (Fig. 7E), ACOX2 expression of protein level (Fig. 7F) and reversed the apoptosis-resistant phenotype (Fig. 7G, Supplementary Fig. 10J). Notably, LPS also upregulated the ECM-associated marker FN1, whereas ACOX2 knockdown attenuated LPS-induced FN1 expression (Supplementary Fig. 10H), supporting a link between ACOX2 and ECM remodeling-associated responses under inflammatory/ROS-associated stress. Consistently, immunohistochemical staining of human prostate tissues demonstrated stronger ACOX2 staining

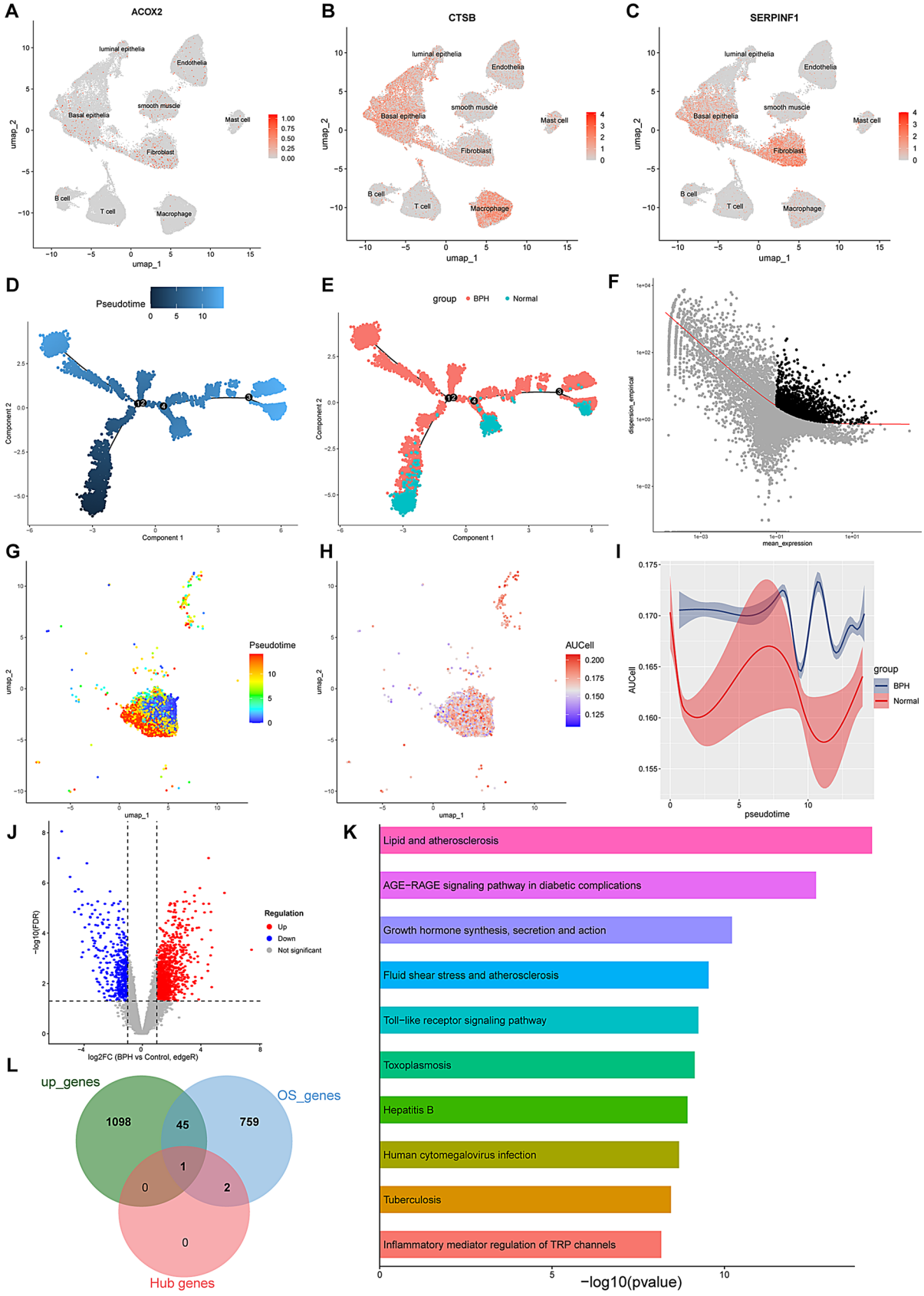

Fig. 4 (See legend on next page.)

(See figure on previous page.)

Fig. 4 Validation of hub genes at the single-cell level and fibroblast heterogeneity in BPH. (**A**–**C**) Expression of ACOX2, CTSB, and SERPINF1 across cells in BPH samples. (**D**) Pseudotime analysis of fibroblasts using Monocle2. (**E**) Distribution of fibroblast developmental trajectories in BPH versus normal samples. (**F**) Genes passing expression and dispersion thresholds. (**G**) Pseudotime distribution of fibroblasts in UMAP space. (**H**) AUCell oxidative stress scores of fibroblasts in UMAP space. (**I**) Persistently higher oxidative stress scores in BPH fibroblasts. (**J**) Differentially expressed genes in fibroblasts between BPH and normal tissues. (**K**) Enrichment analysis highlighting lipid and atherosclerosis and toll-like receptor signaling pathway. (**L**) Overlap of upregulated fibroblast genes in BPH, oxidative stress–related genes, and hub genes identified ACOX2 as a critical gene

in hyperplastic prostate tissue compared with normal prostate tissue (Fig. 7H). Collectively, these results provide experimental support that ACOX2 is induced under oxidative stress and is associated with stromal cell phenotypes consistent with activation (enhanced proliferation and apoptosis resistance), complementing our multi-omics spatial and single-cell findings.

Discussion

Benign prostatic hyperplasia (BPH) is among the most prevalent urological disorders in middle-aged and elderly men. Limited understanding of its pathophysiology has hindered the development of effective therapies. Accumulating evidence implicates oxidative stress (OS) as an important component of BPH-associated pathophysiology [16]. Kaltsas et al. [17] highlighted OS and inflammation as central mechanisms in disease progression, proposing antioxidant and anti-inflammatory strategies as potential adjuncts to standard care. Conversely, Liu et al. [18] demonstrated that HSPA1A may attenuate OS and apoptosis via ERK/JNK signaling, which may be linked to OS and apoptosis-related processes in BPH. Against this background, we sought to clarify the role of OS in BPH, to identify pivotal genes and pathways, and to provide potential molecular targets for novel or combined therapeutic strategies.

Through integrated analysis of two bulk-RNA datasets (GSE7307 and GSE119195), we identified 26 overlapping genes between DEGs, key co-expression modules, and OS-related gene sets. Machine learning approaches consistently converged on three hub genes: ACOX2, CTSB, and SERPINF1, which may serve as candidate biomarkers pending further validation. A nomogram incorporating these genes accurately predicted BPH risk, with robust calibration and ROC performance.

From a clinical perspective, ACOX2, CTSB, and SERPINF1 could be assessed using platforms compatible with routine practice. ACOX2, as an intracellular enzyme, is most feasibly measured in tissue specimens (e.g., TURP chips or biopsy cores) using immunohistochemistry with semi-quantitative scoring (H-score) or RT-qPCR. CTSB and SERPINF1 can be evaluated in tissue by IHC, and given their secreted/extracellular characteristics, they are also potentially measurable using ELISA-based assays in biofluids such as serum or urine, enabling noninvasive or minimally invasive monitoring. Importantly, our biomarkers are proposed as a panel to capture oxidative-stress linked stromal remodeling rather than as stand-alone diagnostic tests. Prospective studies with standardized sampling, quantification, and clinical endpoints will be required to determine incremental value beyond established clinical variables.

Unsupervised clustering stratified BPH samples into two molecular subtypes: C2, enriched for immune activation signatures and characterized by higher immune infiltration; and C1, enriched for neuronal developmental pathways and exhibiting lower immune infiltration. DSigDB-based signature matching highlighted several candidate compounds, including quercetin, a well-known antioxidant. Subsequently, molecular docking was performed, and the binding energies of quercetin with CTSB and SERPINF1 were − 7.9 kcal/mol and − 7.3 kcal/mol respectively, indicating that plausible interactions between top-ranked compounds and CTSB/SERPINF1, which we present as supportive, hypothesis-generating evidence for target engagement rather than proof of therapeutic benefit.

Our findings extend prior bioinformatics-based reports [19] that identified stromal signaling molecules such as BMP5 [20], CXCL13 [21], and NELL2 [22] in BPH, though translation into clinical interventions has remained challenging. The strength of our study lies in the integration of multi-omics with machine learning, enabling precise identification of gene-level biomarkers with therapeutic potential.

Single-cell and spatial transcriptomic analyses provided further insight into cellular heterogeneity. OS scores were elevated across most BPH cell types, with fibroblasts showing the highest levels. Pseudotime analysis revealed persistently increased OS in BPH fibroblasts, and integration with OS-related and hub genes prioritized ACOX2 as a candidate gene associated with OS-high fibroblasts and fibroblast activation trajectories. ACOX2 encodes branched-chain acyl-CoA oxidase, which is involved in the degradation of long-chain fatty acids and bile acid intermediates in the peroxisome [23]. At present, ACOX2 has not been reported in the context of BPH, Tan et al. [24] discovered that ACOX2 is downregulated in prostate cancer (PCa) and is an important indicator for differentiating benign prostate tissues from PCa. We observed an expansion of $ACOX2^{+}$ fibroblasts in BPH (29% vs. 10% in controls), accompanied by enhanced intercellular communication and enrichment of metabolic pathways, including peroxisome metabolism, PPAR signaling, and

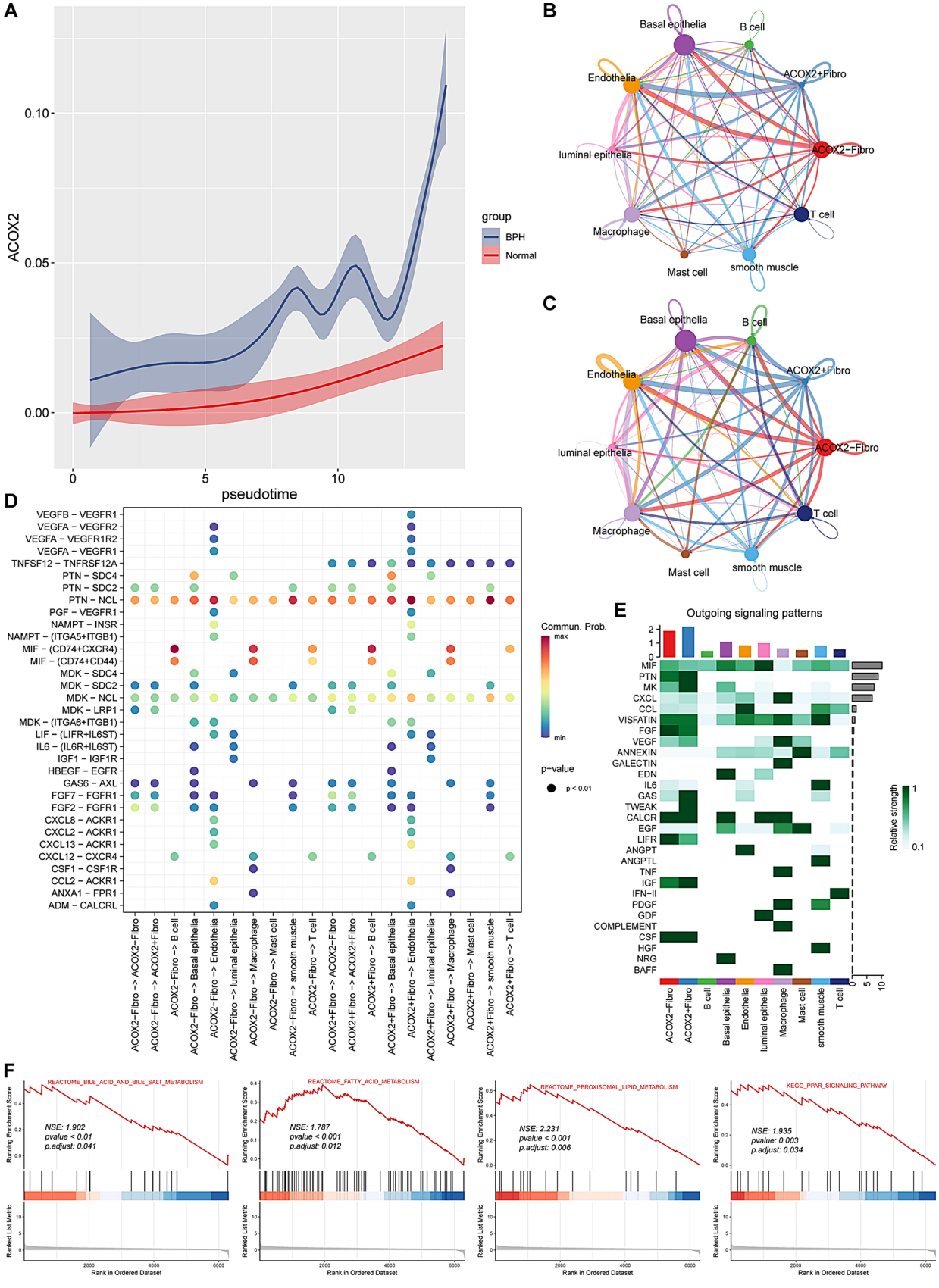

Fig. 5 (See legend on next page.)

(See figure on previous page.)

Fig. 5 Intercellular communication in fibroblast subpopulations. (**A**) Gradual increase of ACOX2 expression along the pseudotemporal trajectory in BPH. (**B**) Cell–cell communication network based on count data. (**C**) Cell–cell communication network based on weight data, with node colors indicating subpopulations and line thickness representing interaction strength. (**D**) Bubble plot of ligand–receptor pairs specifically activated in ACOX2 + fibroblasts. (**E**) Heatmap of communication strength between cell populations, with incoming (top bars) and outgoing (right bars) signal totals. (**F**) GSEA of DEGs in ACOX2 + fibroblasts

fatty acid oxidation. These findings suggest that OS may promote BPH progression by driving fibroblast activation through ACOX2-dependent metabolic reprogramming. This mechanism also provides a plausible link between BPH and metabolic risk factors such as obesity, dyslipidemia, and metabolic syndrome [25–27].

Although RNA velocity can provide additional evidence for the directionality of fibroblast state transitions, robust velocity inference typically requires spliced/unspliced quantification (e.g., loom files or raw alignments) and careful preprocessing. In the present study, the available scRNA-seq resources and our analytical workflow were not optimized for velocity estimation. Therefore, we did not perform RNA velocity to avoid over-interpreting potentially unreliable trajectories. Instead, we inferred fibroblast progression using complementary lines of evidence, including pseudotime analysis showing a gradual increase of ACOX2 along the inferred trajectory, and targeted in vitro perturbation under oxidative stress that supported an ACOX2-linked activation-like phenotype. Collectively, these results support an association between ACOX2-high fibroblasts and activation-related programs while acknowledging that further work with dedicated velocity-ready data would refine developmental directionality.

We acknowledge that LPS is primarily an inflammatory stimulus, and the observed ROS elevation likely reflects downstream inflammatory signaling. To better align with oxidative-stress mechanisms, we additionally tested H_2O_2 as a canonical oxidative-stress inducer and confirmed both ROS increase and ACOX2 induction, supporting that ACOX2 is responsive to oxidative stress per se. In the present study, we used the LPS model for downstream functional assays because it better approximates the inflammatory/ROS-associated micoenvironment relevant to BPH. Although we added an ECM-associated readout (FN1), broader profibrotic remodeling (e.g., COL1A1/ACTA2/TGF-β signaling and in vivo fibrosis phenotypes) still warrants further investigation, and we have therefore maintained cautious language regarding profibrotic causality.

Despite these advances, several limitations remain. Firstly, while we identified correlations between OS activity and the expression of ACOX2, CTSB, and SERPINF1, their precise mechanistic roles in OS regulation require clarification. Future studies should investigate specific signaling pathways modulated by these genes under oxidative stress. Secondly, molecular docking provides a simplified estimate of ligand-protein interaction under static structural assumptions and does not account for protein flexibility, solvent effects, intracellular concentrations, off-target effects, or pharmacokinetics. Therefore, docking scores alone are insufficient to infer therapeutic efficacy or clinical utility. In this study, drug prediction and docking are used to generate testable hypotheses, and future validation will require biochemical binding assays and functional experiments in oxidative-stress relevant prostate stromal models and in vivo BPH models. Thirdly, our findings are based on transcriptomic data from bulk-RNA-seq, scRNA-seq, spatial transcriptomics analyses, and functional validation in cell models, without functional validation in animal models. Experimental confirmation will be essential to establish causality and translational relevance. Lastly, although cross-species validation in rodent BPH models provides supportive evidence for biological robustness, it should be interpreted cautiously and cannot replace independent human cohort validation, given the small rodent sample size and potential differences in prostate biology and disease induction mechanisms between species.

Conclusion

By integrating bulk-RNA-seq, scRNA-seq, and spatial transcriptomics with machine learning, we identified three OS-related hub genes—ACOX2, CTSB, and SERPINF1—with diagnostic potential in BPH. Notably, these findings support an association between oxidative stress, ACOX2 induction, and stromal cell phenotypes consistent with activation; causal relationships and clinical utility require further functional and prospective validation. These findings provide novel insights into the molecular underpinnings of BPH and open avenues for biomarker-driven diagnosis and targeted interventions.

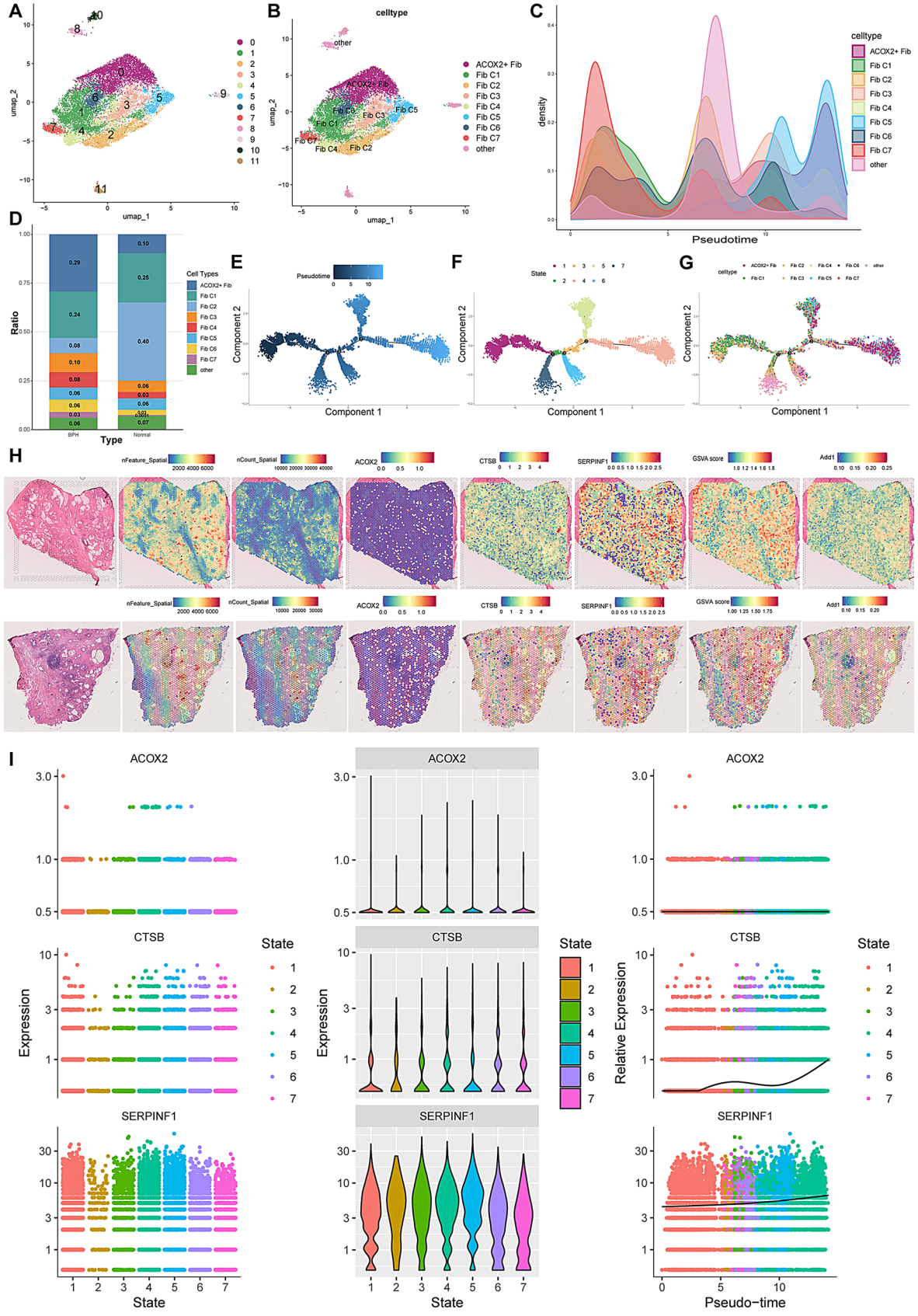

Fig. 6 (See legend on next page.)

(See figure on previous page.)

Fig. 6 Pseudotime trajectory of ACOX2 + fibroblast subtypes and spatial transcriptomic validation. (**A**, **B**) Subclustering of fibroblasts revealed nine subtypes: ACOX2 + Fib, Fib C1–C7, and others. (**C**) Ridge plot of pseudotime trajectories for fibroblast subtypes. (**D**) Proportions of fibroblast subtypes in BPH versus normal tissues. (**E**) Pseudotime analysis showing a continuous process of fibroblast differentiation from quiescent to multiple activated states. (**F**) Division of this process into seven stages. (**G**) ACOX2 + fibroblasts mainly located at terminal branches. (**H**) Spatial co-localization of ACOX2, CTSB, and SERPINF1 expression with oxidative stress scores in BPH samples. (**I**) Dynamic expression changes of the three hub genes along pseudotime

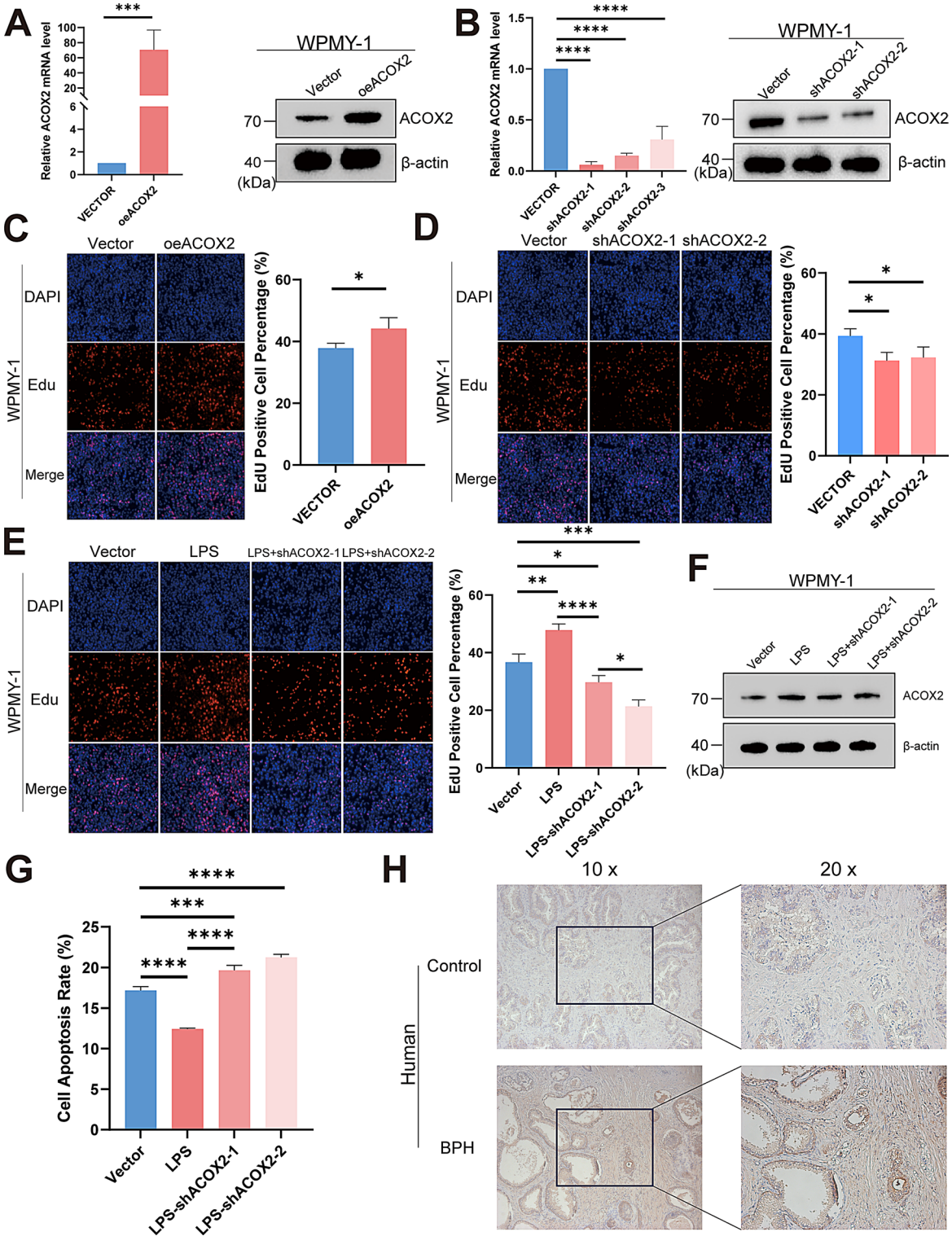

Fig. 7 (See legend on next page.)

(See figure on previous page.)

Fig. 7 ACOX2 modulates proliferation and survival of prostatic stromal cells under oxidative stress and is elevated in BPH tissues. (**A**) Validation of ACOX2 overexpression in WPMY-1 cells. Relative ACOX2 mRNA level (RT–qPCR) and representative western blot showing ACOX2 protein abundance in vector vs. oeACOX2 groups; β-actin served as the loading control. (**B**) Validation of ACOX2 knockdown in WPMY-1 cells. RT-qPCR quantification of ACOX2 mRNA in vector and shACOX2 constructs (shACOX2-1/2), and representative western blot confirming reduced ACOX2 protein. (**C**) EdU proliferation assay in WPMY-1 cells following ACOX2 overexpression. Representative images (DAPI, EdU, merge) and quantification of EdU-positive cells in vector vs. oeACOX2 groups. (**D**) EdU proliferation assay in WPMY-1 cells following ACOX2 knockdown (shACOX2-1/2). Representative images (DAPI, EdU, merge) and quantification of EdU-positive cells. (**E**) EdU proliferation assay under oxidative stress induction. WPMY-1 cells were treated with LPS (20 μg/mL) with/without ACOX2 knockdown (LPS+shACOX2-1/2). Representative images and quantification of EdU-positive cells are shown. (**F**) Representative western blot showing ACOX2 protein levels across vector, LPS, and LPS+shACOX2-1/2 conditions. (**G**) Quantification of apoptosis rate across vector, LPS, and LPS+shACOX2-1/2 groups as assessed by Annexin V-based flow cytometry. (**H**) Immunohistochemical staining of ACOX2 in human prostate tissues. Representative images of normal prostate (Control) and BPH at 10× and 20× magnification; boxed regions indicate the higher-magnification areas. Data are presented as mean ± SD from independent experiments. Statistical significance is indicated as $^{*}P < 0.05$, $^{**}P < 0.01$, $^{***}P < 0.001$, $^{****}P < 0.0001$; ns, not significant

Supplementary Information

The online version contains supplementary material available at https://doi.org/10.1186/s12967-026-08055-8.

Supplementary Material 1

Supplementary Material 2

Supplementary Material 3

Supplementary Material 4

Supplementary Material 5

Supplementary Material 6

Supplementary Material 7

Supplementary Material 8

Supplementary Material 9

Supplementary Material 10

Supplementary Material 11

Supplementary Material 12

Supplementary Material 13

Author contributions

Jie Chen: Conceptualization, Writing– original draft; Jingxing Bai: Formal analysis, Software; Bo Chen: Visualization, Writing– original draft; Yin Huang: Data curation, Writing– original draft; Jinze Li: Formal analysis, Visualization; Jin Li: Formal analysis, Software; Zeyu Chen: Visualization, Software; Biao Ran: Formal analysis, Software; Qiang Wei, Jianzhong Ai, Liangren Liu and Dehong Cao: Investigation, Writing– review & editing. All authors contributed to the article and approved the submitted version.

Funding

This research was funded by the National Natural Science Foundation of China (Grant No. 82170784, No. 82370775, and No.82570905), the West China Hospital High-level Talents Support Program (No. ZYGD23001 and ZYGD24008), and the Key Research Projects of the Ministry of Science and Technology, China (Grant No. 2022YFC3602905).

Data availability

We are grateful for the wealth of bioinformatics data provided by public databases. Detailed information on the databases can be found in Supplementary Table 2. Data are available from the corresponding author upon reasonable request.

Declarations

Ethical approval

This study did not require further ethics committee approval as it is a retrospective study based on a public database.

Consent

This study is a multi-omics study based on a public database and does not involve the privacy of patients, so it was conducted without informed written consent.

Conflict of interest

The authors have no conflicts of interest related to this study.

Author details

[1]Department of Urology, Institute of Urology, West China Hospital, Sichuan University, Chengdu 610041, China

Received: 7 November 2025 / Accepted: 18 March 2026
Published online: 01 April 2026

References

1. Wei JT, Calhoun E, Jacobsen SJ. Urologic diseases in america project: benign prostatic hyperplasia. J Urol. 2008;179:S75–80.
2. The global. regional, and national burden of benign prostatic hyperplasia in 204 countries and territories from 2000 to 2019: a systematic analysis for the Global Burden of Disease Study 2019. Lancet Healthy Longev. 2022;3:e754–76.
3. Nickel JC, Roehrborn CG, O'Leary MP, Bostwick DG, Somerville MC, Rittmaster RS. The relationship between prostate inflammation and lower urinary tract symptoms: examination of baseline data from the REDUCE trial. Eur Urol. 2008;54:1379–84.
4. Roberts RO, Jacobson DJ, Rhodes T, Klee GG, Leiber MM, Jacobsen SJ. Serum sex hormones and measures of benign prostatic hyperplasia. Prostate. 2004;61:124–31.
5. Zarakowska E, Guz J, Gackowski D, Olinski R. Relationship between prostate cancer and benign hyperplasia: role of inflammation-induced oxidative stress, vitamin C, and epigenetics. World J Mens Health 2025.
6. Sanda MG, Beaty TH, Stutzman RE, Childs B, Walsh PC. Genetic susceptibility of benign prostatic hyperplasia. J Urol. 1994;152:115–9.
7. Minciullo PL, Inferrera A, Navarra M, Calapai G, Magno C, Gangemi S. Oxidative stress in benign prostatic hyperplasia: a systematic review. Urol Int. 2015;94:249–54.
8. Vital P, Castro P, Ittmann M. Oxidative stress promotes benign prostatic hyperplasia. Prostate. 2016;76:58–67.
9. Khandrika L, Kumar B, Koul S, Maroni P, Koul HK. Oxidative stress in prostate cancer. Cancer Lett. 2009;282:125–36.
10. Hamid AR, Umbas R, Mochtar CA. Recent role of inflammation in prostate diseases: chemoprevention development opportunity. Acta Med Indones. 2011;43:59–65.
11. Jahan N, Chowdhury A, Li T, Xu K, Wei F, Wang S. Neferine improves oxidative stress and apoptosis in benign prostate hyperplasia via Nrf2-ARE pathway. Redox Rep. 2021;26:1–9.
12. Du C, Wang C, Liu Z, Xin W, Zhang Q, Ali A, Zeng X, Li Z, Ma C. Machine learning algorithms integrate bulk and single-cell RNA data to unveil oxidative stress following intracerebral hemorrhage. Int Immunopharmacol. 2024;137:112449.
13. Leek JT, Johnson WE, Parker HS, Jaffe AE, Storey JD. The sva package for removing batch effects and other unwanted variation in high-throughput experiments. Bioinformatics. 2012;28:882–3.

14. Wu T, Hu E, Xu S, Chen M, Guo P, Dai Z, Feng T, Zhou L, Tang W, Zhan L, et al. clusterProfiler 4.0: A universal enrichment tool for interpreting omics data. Innov (Camb). 2021;2:100141.
15. Lin D, Luo C, Wei P, Zhang A, Zhang M, Wu X, Deng B, Li Z, Cui K, Chen Z. YAP1 Recognizes Inflammatory and Mechanical Cues to Exacerbate Benign Prostatic Hyperplasia via Promoting Cell Survival and Fibrosis. Adv Sci (Weinh). 2024;11:e2304274.
16. Udensi UK, Tchounwou PB. Oxidative stress in prostate hyperplasia and carcinogenesis. J Exp Clin Cancer Res. 2016;35:139.
17. Kaltsas A, Giannakas T, Stavropoulos M, Kratiras Z, Chrisofos M. Oxidative stress in benign prostatic hyperplasia: mechanisms, clinical relevance and therapeutic perspectives. Diseases 2025:13.
18. Liu H, Zhou Y, Wang Z, Liu D, Li Y, Lai H, Qiu J, Shan S, Guo F, Chen P, et al, et al. Heat Shock Protein Family A Member 1A Attenuates Apoptosis and Oxidative Stress via ERK/JNK Pathway in Hyperplastic Prostate. MedComm. 2020;2025(6):e70129.
19. Middleton LW, Shen Z, Varma S, Pollack AS, Gong X, Zhu S, Zhu C, Foley JW, Vennam S, Sweeney RT, et al. Genomic analysis of benign prostatic hyperplasia implicates cellular re-landscaping in disease pathogenesis. JCI Insight 2019:5.
20. Sreekumar A, Simmons MN, Lee TJ, Sharma A, Saini S. Therapeutic potential of pomegranate juice-derived nanovesicles in nude mouse benign prostatic hyperplasia (BPH) xenograft model. Sci Rep. 2023;13:12427.
21. Liu D, Li M, Fu X, Yang S, Wang Z, Liu J, Li Y, Zhou Y, Ren P, Guo Y, et al. Changes in the expression and functional activities of C-X-C motif chemokine ligand 13 (CXCL13) in hyperplastic prostate. Int J Mol Sci 2022:24.
22. Liu J, Liu D, Zhang X, Li Y, Fu X, He W, Li M, Chen P, Zeng G, DiSanto ME, et al. NELL2 modulates cell proliferation and apoptosis via ERK pathway in the development of benign prostatic hyperplasia. Clin Sci (Lond). 2021;135:1591–608.
23. Monte MJ, Alonso-Peña M, Briz O, Herraez E, Berasain C, Argemi J, Prieto J, Marin JJG. ACOX2 deficiency: An inborn error of bile acid synthesis identified in an adolescent with persistent hypertransaminasemia. J Hepatol. 2017;66:581–8.
24. Tan Z, Deng Y, Cai Z, He H, Tang Z, Feng Y, Ye J, Liu R, Cai S, Huang H, et al. ACOX2 Serves as a Favorable Indicator Related to Lipid Metabolism and Oxidative Stress for Biochemical Recurrence in Prostate Cancer. J Cancer. 2024;15:3010–23.
25. Fu X, Wang Y, Lu Y, Liu J, Li H. Association between metabolic syndrome and benign prostatic hyperplasia: The underlying molecular connection. Life Sci. 2024;358:123192.
26. Gacci M, Corona G, Vignozzi L, Salvi M, Serni S, De Nunzio C, Tubaro A, Oelke M, Carini M, Maggi M. Metabolic syndrome and benign prostatic enlargement: a systematic review and meta-analysis. BJU Int. 2015;115:24–31.
27. Vignozzi L, Gacci M, Maggi M. Lower urinary tract symptoms, benign prostatic hyperplasia and metabolic syndrome. Nat Rev Urol. 2016;13:108–19.

Publisher's note